

High-Resolution Shallow Structure along the Anninghe Fault Zone, Sichuan, China, Constrained by Active Source Tomography

Xinru Mu^{1,2}, Junhao Song², Hongfeng Yang^{2,3}, Jianping Huang¹, Huajian Yao⁴, and Baofeng Tian⁵

Abstract

The Anninghe fault (ANHF), located in southwest China, was a major block boundary that hosted M 7.5 earthquakes historically. For seismic hazard assessment, it is critical to investigate fault properties before future earthquakes. To investigate the fault structure, we deployed three linear dense arrays with an aperture of ~ 8–9 km across different segments of the ANHF from October 2019 to March 2020. More importantly, we detonated a new methane source to generate seismic waves, which is environmentally friendly and can be used in different regions such as mountainous and urban areas. After data acquisition, we first removed the noise to accurately pick up the first arrivals of seismic waves. Then, we conducted the first-arrival seismic tomography, a method commonly used in the petroleum industry, to obtain the high-resolution *P*-wave velocity structure. The tomographic results showed distinct low-velocity zones (LVZs) of ~ 1000–1500 m in width and ~ 300–400 m in depth along the fault, well consistent with the lateral distribution of site amplification that was derived from regional earthquake waveforms. These LVZs may have formed as a combined result of the fault damage zone and ANHF-controlled sediments. As the Anning River Valley is densely populated, our newly identified LVZs shed lights on earthquake hazard in the region. In addition, we demonstrate that using a combination of methane detonation sources, linear dense arrays, and active source tomography can effectively determine the shallow *P*-wave velocity model in complex environments (i.e., mountains and urban areas).

Cite this article as Mu, X., J. Song, H. Yang, J. Huang, H. Yao, and B. Tian (2023). High-Resolution Shallow Structure along the Anninghe Fault Zone, Sichuan, China, Constrained by Active Source Tomography, *Seismol. Res. Lett.* **XX**, 1–13, doi: [10.1785/0220230137](https://doi.org/10.1785/0220230137).

[Supplemental Material](#)

Introduction

Rock fragmentation and damage caused by fault slip and earthquake ruptures usually accumulate into a near-fault damage zone (FDZ), which often has complex structural characteristics (Ben-Zion and Sammis, 2003; Yang, 2015). It is critical to study the structural and velocity properties of the FDZ, which hold a great deal of information to understand fault evolution and assess future earthquake hazards. Compared with the intact host rock, the seismic-wave velocity of the damage zone is lower, and thus it is usually called a low-velocity zone (LVZ; Yang, 2015). Because of their relatively high porosity, LVZs may become channels for fluid migration, and the fluids migrating to the fault plane can reduce the frictional resistance on fault, increasing the likelihood of earthquake generation (Faulkner *et al.*, 2010; Yehya *et al.*, 2018). Furthermore, LVZs in the vicinity of a fault have the potential to alter seismic rupture modes (Harris and Day, 1997; Huang and Ampuero, 2011; Weng *et al.*, 2016) and amplify ground shaking (Wu *et al.*, 2009; Kurzon *et al.*, 2014; Pratt *et al.*, 2017; Song and Yang, 2022). According to the results of dynamic rupture simulation,

the LVZ will promote rupture and slip on fault (Chen and Yang, 2020; Yang *et al.*, 2022), and the promotional extent will increase with the width and depth of the LVZ (Weng *et al.*, 2016). Moreover, the time-dependent variation of velocity in the LVZ can be used as evidence of fault healing, which is of great significance to the study of earthquake cycles and evolution of fault systems (Yang, 2015; Yang *et al.*, 2021). Therefore, deriving high-resolution fault zone (FZ) structure holds significant implications in understanding earthquake mechanics.

1. Geosciences Department, China University of Petroleum (East China), Qingdao, Shandong, China; 2. Earth System Science Programme, Faculty of Science, The Chinese University of Hong Kong, Shatin, Hong Kong, China,  <https://orcid.org/0000-0003-2706-0778> (JS);  <https://orcid.org/0000-0002-5925-6487> (HY);
3. Shenzhen Research Institute, The Chinese University of Hong Kong, Shenzhen, China; 4. Laboratory of Seismology and Physics of Earth's Interior, School of Earth and Space Sciences, University of Science and Technology of China, Hefei, Anhui, China;
5. Institute of Geophysics, China Earthquake Administration, Beijing, China

*Corresponding author: hyang@cuhk.edu.hk

© Seismological Society of America

Many seismic imaging methods based on dense arrays have been developed and applied to image the LVZ across different FZs. The commonly used methods include the analysis of travel times and waveforms of FZ trapped waves (Ben-Zion *et al.*, 2003; Cochran *et al.*, 2009), head waves (McGuire and Ben-Zion, 2005), and FZ-reflected body waves (Li *et al.*, 2007; Yang and Zhu, 2010), which have been applied to FZ studies in different regions of the world. With the development of dense nodal arrays containing small interstation spacing distance and large aperture, passive source body-wave tomography (Allam *et al.*, 2014), ambient noise tomography (Wang *et al.*, 2019; Zigone *et al.*, 2019; Yang *et al.*, 2020; Li *et al.*, 2021; Luo *et al.*, 2023), as well as joint inversions of seismic and magnetotelluric data (Xu *et al.*, 2021) have been recently developed in imaging LVZs. By far, the width of the LVZ can be well constrained from dense array recordings and often falls within the range of a few hundreds to thousands of meters (Li and Malin, 2008; Cochran *et al.*, 2009; Yang, 2015; Yang *et al.*, 2020). In comparison, constraining the depth extent of the LVZ is more challenging and sometimes leads to debate (Li and Vernon, 2001; Ben-Zion *et al.*, 2015). By taking advantage of the high vertical resolution of the teleseismic receiver function, Jiang *et al.* (2021) proposed a dense-array-based inversion method that was effective in determining the LVZ depth.

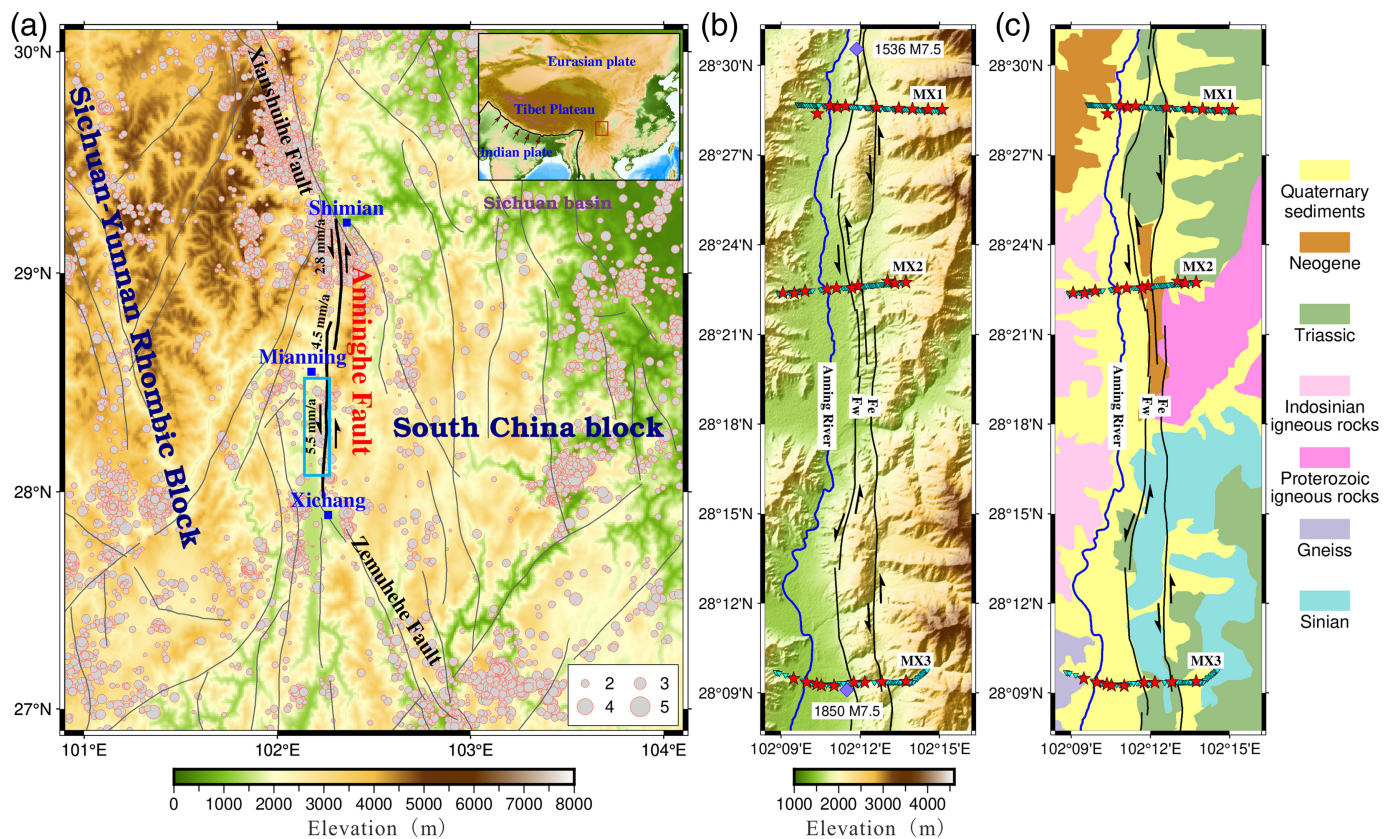
In addition to passive source methods, active sources have also been used to derive FZ structure. For instance, large-volume-explosion-generated reflection and refraction data were used to study the structure of the San Andreas fault near Parkfield (Hole *et al.*, 2006; Bleibinhaus *et al.*, 2007). Because of the large shot spacing (varying from 0.2 to 3 km), however, this experiment cannot precisely image the structure of the shallow FZ. Lay *et al.* (2020) combined densely distributed vibroseis (with source spacing of tens of meters) and receivers (with receiver spacing of tens of meters) to image the New Zealand Alpine fault and obtained a detailed 3D velocity structure to 1 km depth. Because active sources are often located at the surface and could generate high-frequency seismic data, they are ideal for high-resolution imaging of the shallow subsurface structure (Virieux and Operto, 2009), and thus are frequently used in industrial production to detect oil and gas resources (Virieux and Operto, 2009; Smithyman and Clowes, 2012). In addition, large-volume air-gun arrays in lakes have nearly identical repeated signals and are thus used to monitor the time-varying characteristics of FZ properties (e.g., Yang *et al.*, 2021; Luan *et al.*, 2023). This type of active source, however, can only be excited in a specific body of water with limited application scenarios. Because of the high cost of active source data acquisition and the limited application scenarios of existing artificial sources, it is still quite limited to apply active source methods to derive the structure of the FZ.

Recently, a new methane detonation source has been developed (Ji *et al.*, 2021). Comparing with traditional active sources, the new methane detonation source has many advantages, such

as no environmental pollution, low cost, and suitability for complex environments (e.g., mountains and urban areas), allowing the active source method to be widely used to study shallow FZ structures (e.g., Zhang *et al.*, 2023). From October 2019 to March 2020, we deployed three linear dense arrays across the Anninghe fault (ANHF; Fig. 1)—one of the major block boundaries between the Sichuan–Yunnan rhomboid block and the South China block. Although the number of present local seismicity is low, the ANHF had hosted several historical large earthquakes with magnitudes greater than 7 (Wen, Fan, *et al.*, 2008) and may experience M_w 7+ earthquakes in the future (Yao and Yang, 2022). In addition to recording earthquakes, we excited a total of 28 shots along the three linear dense arrays using the new methane detonation source. Based on the P -wave first-arrival times and double-difference tomography, Shao *et al.* (2022) derived shallow velocity structures along the ANHF. However, the large mesh grids (several hundred meters) during their tomographic inversion introduced significant limits in imaging the fine structure of the FZs. In this study, a high-resolution tomography method commonly used in the petroleum industry was introduced. The obtained high-resolution shallow structures were in good agreement with seismic site response. Our results advanced our understanding of the evolution of the ANHF and shed critical light on future seismic assessment for potentially amplified ground motions during future large earthquakes.

Tectonic Setting and Data

In southwest China, the collision of the Indian plate with the Eurasian plate has resulted in a large number of faults and seismic activity (Yang *et al.*, 2020). In the southeastern margin of the Qinghai–Tibet Plateau, the Xianshuihe–Anninghe–Zemuhe fault system lies between the Sichuan–Yunnan rhombic block and the South China block, and has hosted numerous large earthquakes, including the recent devastating 2022 M_w 6.6 Luding earthquake (An *et al.*, 2023; Hu *et al.*, 2023; Qu *et al.*, 2023; Xie *et al.*, 2023). The ANHF extends in roughly north–south direction for ~ 150 km from Shimian in the north to Xichang in the south (Fig. 1a). It is a left-lateral strike-slip fault with an increasing slip rate from north (2.8 mm/yr) to south (5.5 mm/yr) (Tan *et al.*, 2018). According to historical records, the most recent large earthquake was an M 7.5 event north to Xichang in 1536. It has been suggested that the recurrence interval of M 7 earthquakes on the ANHF is ~ 400 – 600 yr (Wen, 2000; Tan *et al.*, 2018), and the Mianning–Xichang segment is a maturing seismic gap with a looming large earthquake (Wen, Fan, *et al.*, 2008; Wen, Ma, *et al.*, 2008; Ran *et al.*, 2008). Present seismicity is low (Yi *et al.*, 2004), consistent with the present interseismic locking distribution along the ANHF (Jiang *et al.*, 2015). Based on dynamic rupture simulations, Yao and Yang (2022) predicted that future earthquakes on the ANHF may have moment magnitudes ranging from 6.9 to 7.3, with a high likelihood of surface rupture



causing severe ground motion in densely populated areas such as Mianning and Xichang. Therefore, it was critical to investigate the structure of the ANHF (Fig. 1a) to better understand fault properties and assess future earthquake hazards. Because of few local earthquakes along the ANHF, it was ideal to derive high-resolution images of the FZ using active source data.

Recent experiments have proved that dense across-fault arrays with a large aperture and small interstation spacing can help us better constrain the structures of the LVZs (Share *et al.*, 2017; Yang *et al.*, 2020; Jiang *et al.*, 2021; Song and Yang, 2022). As such, we have deployed three dense across-fault arrays across the Mianning–Xichang segment of ANHF from October 2019 to March 2020, covering the two fault strands (Fig. 1b). The west and east branch faults were named F_w and F_e , respectively. To the west of the west branch fault was the Anning River Valley. The three arrays were roughly perpendicular to the geologically inferred fault traces. From northwest to southeast, the three arrays MX1, MX2, and MX3 (Fig. 1b) were each equipped with 109 (QS-10: 10 s–250 Hz effective frequency band, 100 Hz sampling rate, 3C type), 80 (QS-5A: 5 s–250 Hz effective frequency band, 100 Hz sampling rate, 3C type), and 75 (PMS-10: 10 s–150 Hz effective frequency band, 500 Hz sampling rate, 3C type) short-period instruments with a distributed aperture of 9, 8, and 9 km, respectively. For arrays MX1, MX2, and MX3, the interstation spacings are ~ 70 m, ~ 100 m, and ~ 100 m, respectively.

In addition, we detonated a methane source, a new type of environmentally friendly artificial source (Ji *et al.*, 2021; Zhang

Figure 1. (a) Topographic map and the distribution of faults (gray lines) in southwestern China. The thick black line shows the surface trace of the Anninghe fault (ANHF; Tan *et al.*, 2018). The arrows show the slip direction of the strike-slip fault, and the average slip rates of different sections are also marked. The gray dots denote earthquakes with magnitudes greater than 1 since 2018 (data were obtained from the Sichuan Earthquake Administration). The inset map shows the Tibetan plateau, where the study area is marked by a red box. The skyblue box restrains the boundary of panels (b) and (c). Panels (b) and (c) show the topographic map and geological mapping (modified after Shao *et al.*, 2022) of the studied ANHF region, respectively. They show the locations of the Anning River (blue line), geologically inferred branch faults (black lines), methane detonation sources (red stars), across-fault dense linear arrays (cyan triangles), and the surface rupture zone caused by historical earthquakes (purple diamonds) (Cheng *et al.*, 2010). The color version of this figure is available only in the electronic edition.

et al., 2023), to generate seismic waves. When working in the field, the source cavity was first placed in a predrilled well, and then a mixture of methane and oxygen was injected into it (Fig. 2a). An initiation system ignited the methane gas in the cavity, generating seismic waves that traveled downward because of the high-pressure gas released from the bottom of the cavity. The detonation reaction was restricted to the steel cavity and did not result in secondary disasters like those caused by explosive sources. Furthermore, because of its small volume, low drilling cost, and high construction efficiency, it

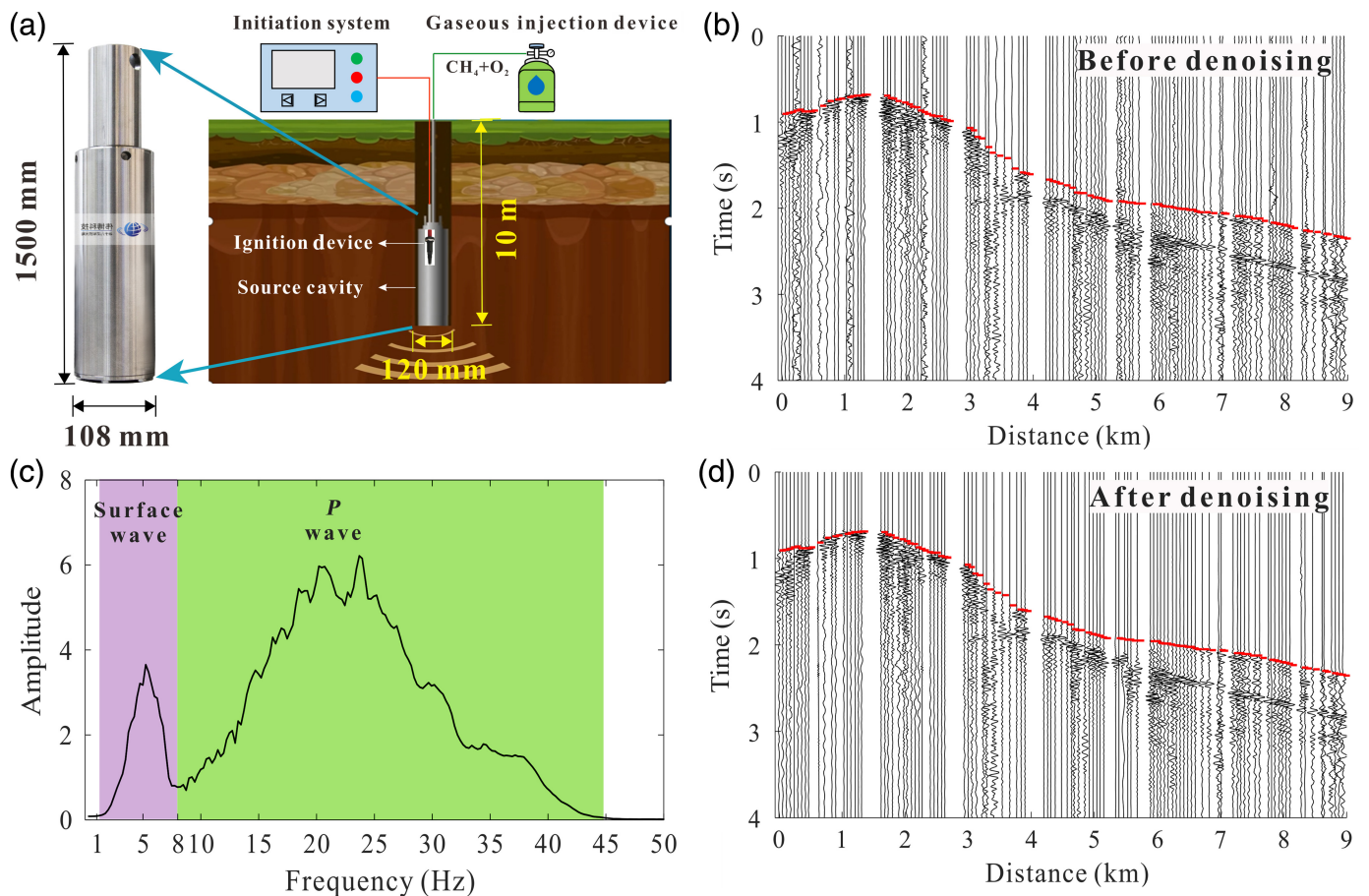


Figure 2. Methane detonation source and acquired shot gather. (a) Instrument and field operation, (b) acquired raw data from shot B02, (c) amplitude spectrum of panel (b), and (d) denoised data for panel (b). Note that the position of the westernmost station represents zero. The color version of this figure is available only in the electronic edition.

can be widely used in mountainous areas, urban areas, and other complex environments.

In this experiment, we obtained a total of 28 2D common-shot gathers by detonating 9, 10, and 9 methane sources (red stars in Fig. 1b) along MX1, MX2, and MX3, respectively. The name, position, and excitation time for all shots can be found in Table S1, available in the supplemental material to this article. As shown in one raw data of the acquired common-shot-gather from shot B02 (Fig. 2b), the horizontal propagation distance of seismic waves generated by the methane source can reach at least 9 km (Fig. 2b). Figure 2c showed the spectra of the data. The frequency distribution range of the *P*-wave signal was 8–45 Hz, much higher than the surface wave (less than 8 Hz). These high-frequency *P* waves ensured that we could get high-resolution shallow velocity structures.

Methods and Results

Noise mitigation and first break picking

Before collecting the first arrivals of seismic waves, we applied a wavelet-transform-based seismic denoising method to the acquired data (Mousavi and Langston, 2016). This method estimates noise characteristics prior to first-arrival times and then removes background noise with similar characteristics from the effective signal. To do so, we roughly picked the first arrival on each channel and then used the data prior to the

first-arrival wave with a time window of 10 s to calculate the background noise level. Then a soft thresholding function was used to mitigate the noise.

After denoising, the weak first arrivals in the raw data of the shot B02 were clearly enhanced (Fig. 2d), improving the accuracy of our picked arrivals. Because we focus on the active source waveforms that have a small amount of seismic data, we conduct manual pickup of first arrival rather than automatic methods, which need to be double checked and validated by manual inspection. In total, there were 693, 749, and 532 first arrivals for MX1, MX2, and MX3, respectively.

First-arrival travel-time tomography results

Based on the picked *P*-wave arrivals, we derived shallow *P*-wave velocity structures using the parallel fast sweeping method based adjoint seismic tomography (PFAST)—a commonly used method of first-arrival seismic tomography in oil

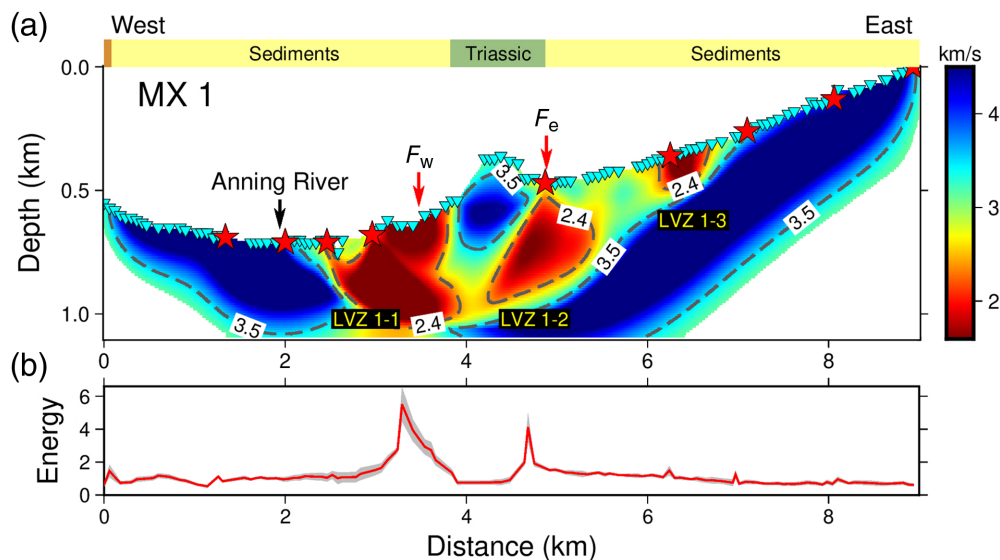


Figure 3. *P*-wave velocity models and site amplification analysis across MX1. Panel (a) displays the velocity model beneath the array MX1, and local geology maps associated with the MX1 are put on the upper part. The black arrow shows the location of the Anning River. The red arrows denote the locations of the western and eastern branches of the ANHF. The cyan triangles and red stars represent receiver and shot positions, respectively. The obtained low-velocity zones (LVZs) are numbered and marked in (a). Note that the position of the westernmost station represents zero, and the regions with sparse ray coverage were muted. Panel (b) shows the calculated average energy (red line) of the trapped wave and the corresponding standard deviation (gray). The color version of this figure is available only in the electronic edition.

and gas exploration (Huang and Bellefleur, 2012). Compared to the traditional ray tracing method, this method uses a grid-based Eikonal equation solver to calculate travel time, and thus avoids the problems of shadow zones and caustic regions. In addition, this method can process field data with irregular topography, which was applied on all our three lines. To avoid a large amount of computation in estimating the Fréchet derivative matrix for a large-scale problem, the PFAST used the adjoint state method to calculate the gradient of the L_2 norm, which can be written as

$$E(v) = \frac{1}{2} \|T(\mathbf{x}_r; \mathbf{x}_s) - T_o(\mathbf{x}_r; \mathbf{x}_s)\|^2, \quad (1)$$

in which v denotes the propagation velocity of seismic waves, $T(\mathbf{x}_r; \mathbf{x}_s)$ is the synthetic travel time at the receiver located at \mathbf{x}_r for a source located at \mathbf{x}_s , and $T_o(\mathbf{x}_r; \mathbf{x}_s)$ is the observed travel time.

As shown in Figure 1b, three survey lines were nearly linear and were therefore assumed to be three 2D geometric straight lines during tomographic inversion. Here, we chose the initial velocity models that linearly increased from the top to the bottom of our model domain (Fig. S1). These models were discretized using a 10 m grid in both horizontal and vertical directions, which was also used during inversion. To ensure the stability and accuracy of the model, we chose the same regularization

parameters (smoothness factors) for the three survey lines, which were 280 and 150 in the horizontal and vertical directions, respectively. For PFAST, the choice of regularization parameters is usually made after a few trial runs. Therefore, we adjust these two regularization parameters until we get the optimal inversion velocity model.

The results of checkerboard tests revealed that the PFAST can recover anomalies as small as 400×200 m (Figs. S2–S4). Furthermore, the PFAST could recover velocity characteristics at depths of up to 500 m. By implementing tomographic inversion, shallow velocity structures beneath the three lines (Figs. 3–5) were obtained. Both the small convergence values of the final root mean square (rms) misfits (Fig. 6) and the consistent fit between the

observed first arrivals, and the synthetic first arrivals calculated by the final inverted velocity model (Fig. 7) validated the accuracy of the imaging results. It should be noted that, due to the selection of large regularization parameters, the dependence of the inversion method on the initial velocity model is reduced. Therefore, even if the initial velocity model (Fig. S1) differs significantly from the real velocity model, the final inversion results are still reliable, which is proved by the residual convergence curve (Fig. 6) and the comparison between the simulated and observed first arrivals (Fig. 7). We also note that the data match well with the simulations at near offsets, but the match gets worse at far offsets (Fig. 7). This is due to the poor quality of the seismic data at far offsets, which prevents us from picking the first arrivals at every seismic trace for each shot. In fact, we are able to pick up the first arrivals at near offsets for each shot but only obtain the first arrivals at far offsets for some of them. Because of the lack of first arrivals, the velocity information constrained by far offsets is less accurate. As a result, there is a discrepancy between the synthesized first arrivals and the observed first arrivals at far offsets.

The velocity values beneath the three arrays were in the range of ~ 1.6 – 4.5 km/s, all consistent with each other. Furthermore, our velocity profiles showed that distinct LVZs with *P*-wave velocities of 1.6–2.4 km/s were distributed across the linear dense arrays (Figs. 3–5). In contrast, surrounding materials all had V_p larger than 3.5 km/s, which was used to delineate the velocity boundary (Figs. 3–5). Beneath the northern array

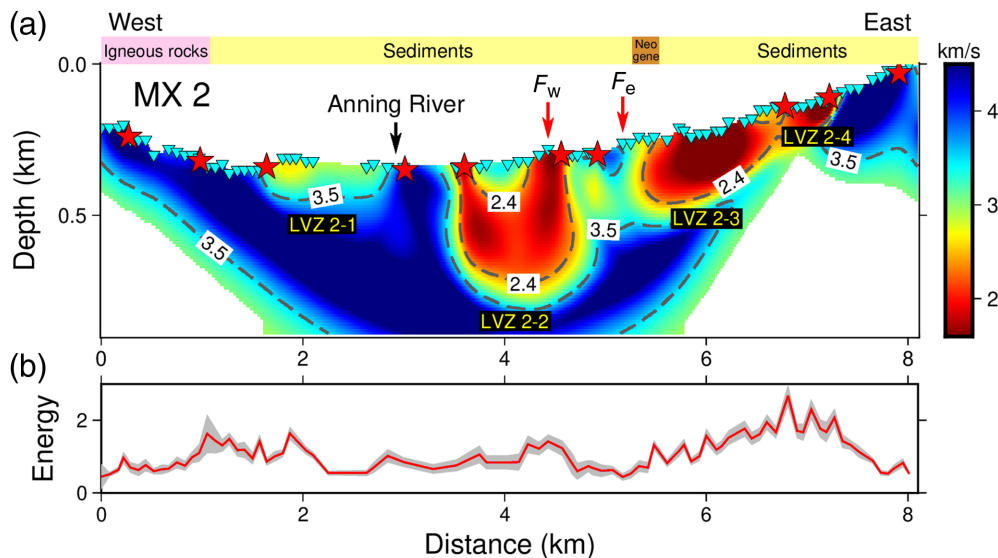


Figure 4. *P*-wave velocity models and site amplification analysis across MX2. Panel (a) displays the velocity model beneath the array MX2, and local geology maps associated with the MX2 are put on the upper part. Notions are the same as in Figure 3a. Panel (b) shows the calculated average energy (red line) of the trapped wave and the corresponding standard deviation (gray). The color version of this figure is available only in the electronic edition.

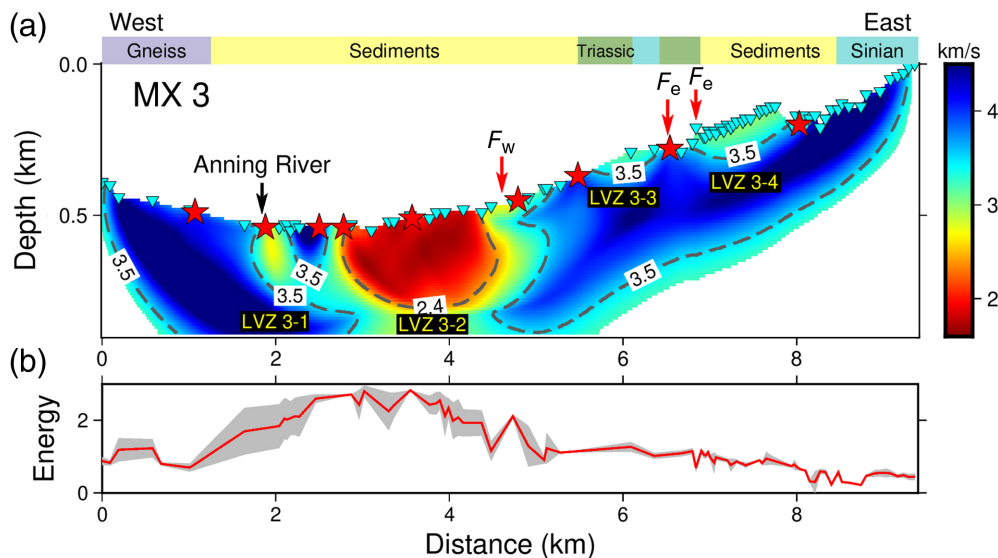


Figure 5. *P*-wave velocity models and site amplification analysis across MX3. Panel (a) displays the velocity model beneath the array MX3, and local geology maps associated with the MX3 are put on the upper part. Notions are the same as in Figure 3a. Panel (b) shows the calculated average energy (red line) of the trapped wave and the corresponding standard deviation (gray). The color version of this figure is available only in the electronic edition.

MX1, for instance, two LVZs with *P*-wave velocities of less than 2.4 km/s were found along the mapped fault traces (Fig. 3a). The LVZ 1-1, with a width of ~ 1.4 km, was associated with the western trace F_w and appeared to distribute asymmetrically, whereas the LVZ 1-2 was symmetrically distributed around

the eastern fault trace F_e on both sides, having a width of ~ 1 km. The two LVZs extended to depths of ~ 400 m (Table S2). In between, the two LVZs laid one zone associated with the local topography and geology, having *P*-wave velocities higher than 3.5 km/s (Fig. 3a). The velocity reduction of the LVZs was at least $\sim 31\%$. On the east side of the LVZ 1-2, there existed a LVZ 1-3 with a smaller width (700 m) than those of the LVZs 1-1 and 1-2. The depth extent of the LVZ 1-3 is around 200 m.

Similarly, we also found two LVZs along the mapped fault traces beneath the middle array MX2 (Fig. 4a). The LVZ 2-2 was 1.1 km in width and was asymmetrically distributed on the west side of the fault trace F_w , extending to ~ 400 m in depth. The LVZ 2-3 was also asymmetrical along the fault trace F_e , but it was mainly distributed on the east side of the fault. Compared with the LVZ 2-2, the width was similar but the depth extent of the LVZ 2-3 was shallower, no more than 240 m (Fig. 4a). LVZ 2-4, with a smaller width (500 m) and shallower depth (200 m), existed further east of the model domain. In addition, we also found a shallow LVZ on the west side of the Anning River (LVZ 2-1 in Fig. 4a), with velocity values of 2.6–3.5 km/s, greater than that of the LVZs beneath the fault traces. Chen *et al.* (2023) used the horizontal-to-vertical spectral ratio method to study the depth of the LVZ of arrays MX1 and MX2, and estimated that there was a low-velocity interface near the valley at depths of 300–600 m. This is consistent with the findings of this article. Along the southern array MX3, we also observed a LVZ beneath the Anning River (Fig. 5a). Compared with the

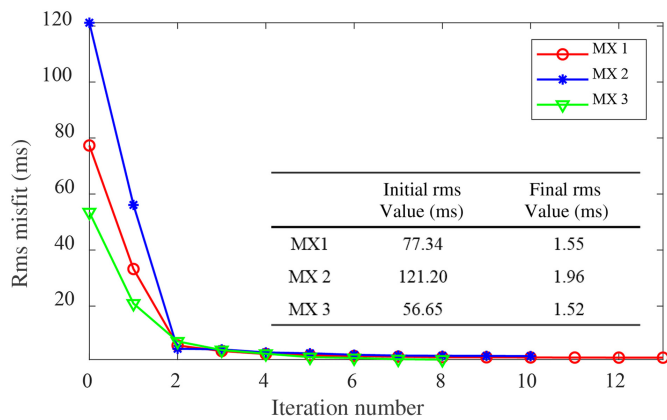


Figure 6. The root mean square (rms) misfit for the first-arrival travel-time tomography as a function of iteration number, for which the red, blue, and green lines show the arrays of MX1, MX2, and MX3, respectively. The initial and final rms values are also shown. The color version of this figure is available only in the electronic edition.

LVZ 2-1, the width of the LVZ 3-1 was smaller, but the depth extent was larger. The most prominent feature beneath the MX3 was the LVZ 3-2, which was distributed asymmetrically along the fault trace F_w with a width of ~ 2 km by tracing the velocity contour of 2.4 km/s (Fig. 5a). The LVZs 3-1 and 3-2 were separated at depths less than 200 m but connected at greater depths. To the east, LVZs 3-3 and 3-4 with shallow depths were found on both sides of the fault trace F_e . The LVZs adjacent to the fault trace F_e in array MX3 exhibit higher velocity values compared to the LVZs near the fault trace F_e observed in arrays MX1 and MX2. This phenomenon may arise due to the simplification that the curvature of the array MX3 was ignored in tomography inversion.

Site amplification analysis

To further validate our velocity models, we conducted site amplification analysis beneath each linear array. Seismic waves could be trapped and significantly amplified when they travel from the surrounding high-speed medium into shallow LVZs (Lewis *et al.*, 2005; Kurzon *et al.*, 2014). In addition, the spatial variation in seismic site amplification has been observed to correlate well with the near-surface structure and thus could be used to effectively constrain the width of the LVZ structure (Wang *et al.*, 2019; Song *et al.*, 2022). Therefore, we investigated the shallow subsurface LVZ structure by conducting analysis of seismic site amplification.

Here, we followed the method described by Wang *et al.* (2019) to calculate the seismic site amplification across the three arrays. This method uses the energy summation of trapped waves below 3 Hz to reveal the width of the coherent FDZs. During our deployment period, a total of seven local earthquakes (Fig. 8) with high signal-to-noise ratios and epicentral

distances less than 200 km were analyzed. To alleviate the influence of environmental and man-made noise, we also used the wavelet-transform-based denoising method to mitigate noise in seismic data (Fig. 9). Then, for each vertical-component waveform, we applied a 0.2–3 Hz band-pass filter and calculated its energy, which was the integral of the squared envelope of the recorded seismic P and S waves from the event origin time with a time window twice of the P -arrival time. Following that, we normalized the energy across the array by the media energy for each event, and calculated the mean energy and standard deviation (st. dev.) of all the selected events.

The standard deviation values for all three energy profiles were small (Figs. 3–5), indicating that the seven events had similar energy amplification pattern. The mean energy distribution of array MX1 (Fig. 3b) showed two distinct zones with obvious site amplifications, which matched well with the LVZs distributed beneath the fault traces (Fig. 3a). There was localized slight energy amplification at distances between 6 and 8 km in the vicinity of the LVZ 1-3 (Fig. 3b). The energy amplification of array MX2 mainly consisted of three parts (Fig. 4b). The first amplification zone was located at a distance of about 2 km, corresponding to the LVZ 2-1. The second part was located at an across-profile distance of about 4 km, and its boundary corresponded well with the boundary of the LVZ 2-2. The third part existed at a distance between 5 and 8 km, and matched well with the LVZs 2-3 and 2-4. However, the amplitude amplification ratio beneath the MX2 was much smaller than that of the MX1. For array MX3, energy amplification existed at a distance between 1 and 5 km, which had a good correspondence with the LVZs 3-1 and 3-2 (Fig. 5b). Because the velocity difference between LVZs 3-3 and 3-4 and the surrounding rock was small, the energy amplification in this area was rather minor. In conclusion, seismic amplification analysis and tomography results were quite consistent with each other.

Discussion

Distribution of LVZs beneath the Anning River Valley

From the tomographic imaging results along the ANHF, we found that there were LVZs with a width of ~ 1000 – 1500 m and a depth of ~ 300 – 400 m beneath the two fault branches (Figs. 3–5). The width of the LVZ caused by past earthquakes was usually only a few hundred meters (Yang, 2015). For example, LVZs of a few hundred meters in width were found along the Landers fault (Peng *et al.*, 2003; Li *et al.*, 2007), the Lavic Lake fault (Li *et al.*, 2002), the San Andreas fault (Li and Malin, 2008), the San Jacinto fault (Yang and Zhu, 2010), and the Longmenshan fault (Li *et al.*, 2013). LVZs with widths greater than 1 km were rare, with only two reports to date. The first report described long-lived fault damage along the Calico fault that resulted in a 1.5 km wide LVZ (Cochran *et al.*, 2009). The second one was discovered with a width of 3.4 km along

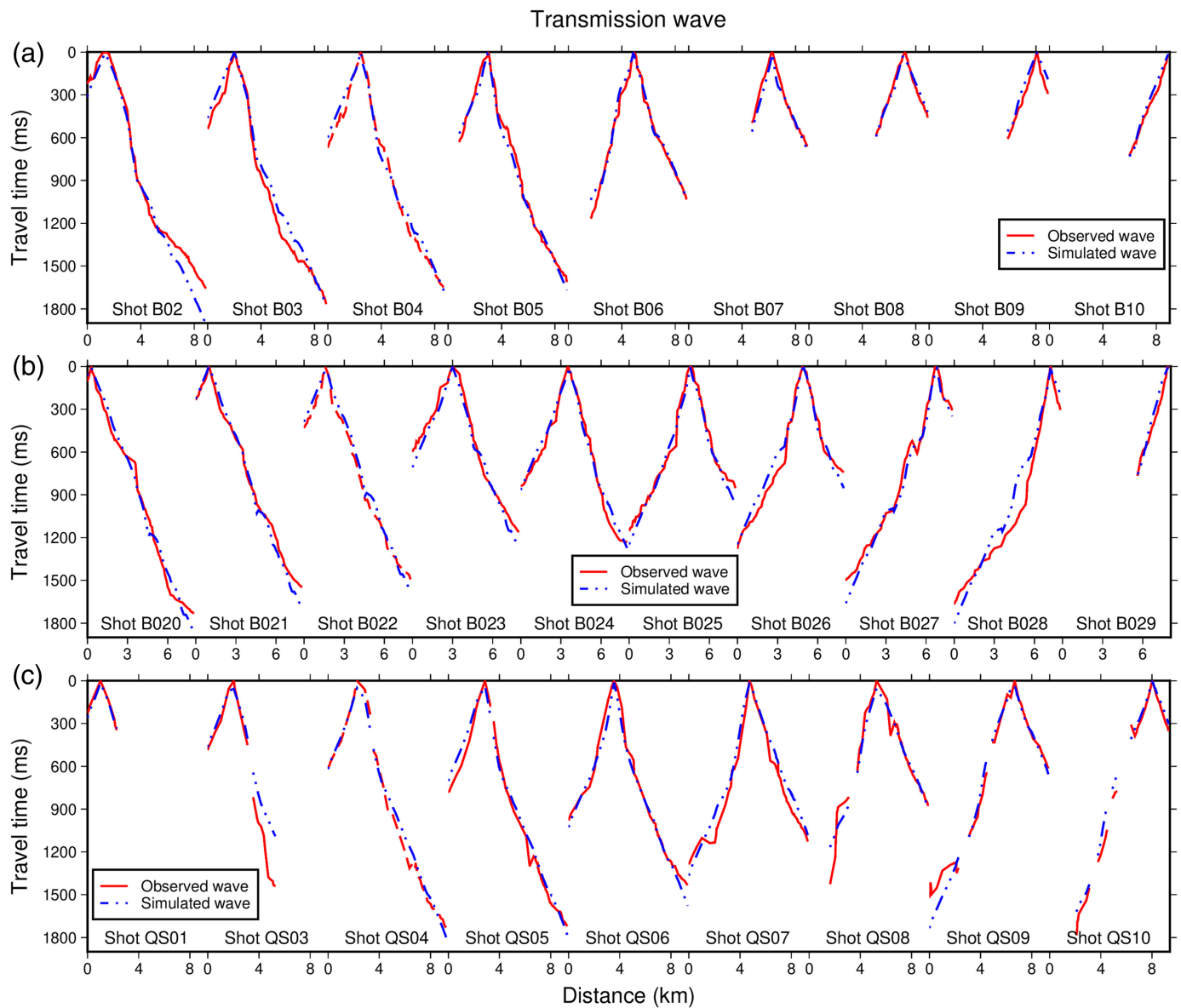


Figure 7. Comparison between the observed first arrivals (red lines) and the synthetic first arrivals (blue lines) that are computed by the tomographic velocity models. Panels (a), (b), and (c) display the first arrivals from arrays MX1, MX2, and MX3, respectively. The color version of this figure is available only in the electronic edition.

the Chenghai fault, which was interpreted as a result of fault-controlled sediment deposit (Yang *et al.*, 2020; Zhang *et al.*, 2023).

The ANHF was an active fault with both sinistral strike-slip and thrust components. It had an estimated average slip rate of 5.5 mm/a in our study region (Cheng *et al.*, 2010). There have been a number of moderate-to-large magnitude earthquakes that occurred along the ANHF. For instance, surface rupture caused by the 1536 M 7.5 earthquake was found to the north of our array MX1 (Fig. 1b). Moreover, another surface rupture caused by the 1805 M 7.5 earthquake was discovered near array MX3 (Fig. 1b). Such large earthquakes should no doubt have contributed to the generation of the LVZs beneath the ANHF. However, the LVZs beneath the ANHF were more than 1 km wide and may not be formed only by historical earthquakes. Indeed, the ANHF in the region was the controlling factor of Anning River Valley basin, which was formed during middle and late Pleistocene (Zhang *et al.*, 2004). There were two major

FZs in the region, and quaternary deposits were abundant around them (Fig. 1c). As a result, we interpreted the LVZs beneath the ANHF fault branches to be the composite of the ANHF-controlled sediments and the FDZ.

The velocity values of LVZs (i.e., LVZs 1-3 and 2-4) that were located at the most eastern end of the velocity profile were similar to those found beneath fault traces. Their formation may be related to the slip and sediment accumulation of a hidden strike-slip fault, which was named F_p here. The Anning River was a large river with an average width of 73 m and abundant water all year round. Throughout history, the continuous

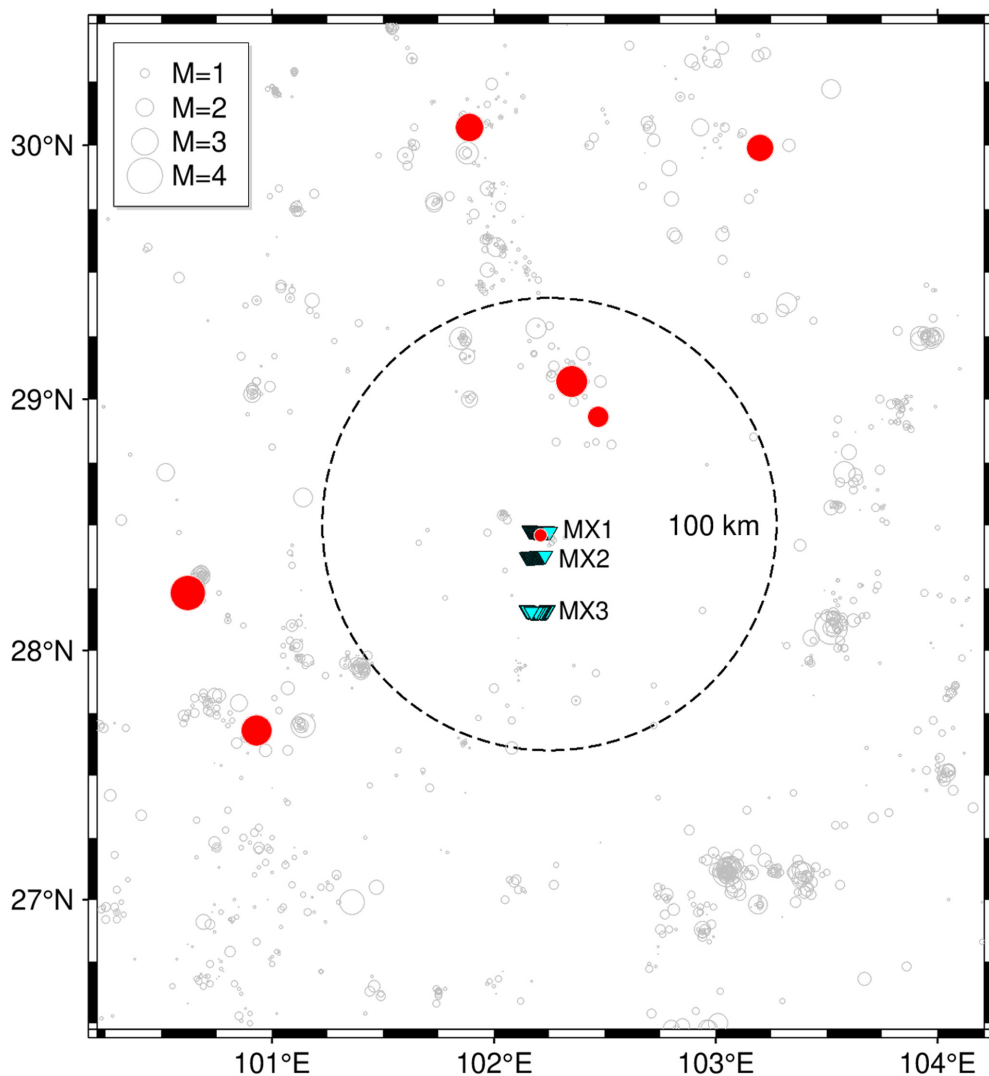


Figure 8. The distribution of seven local earthquakes (red dots) that were used in the site amplification tests. The white dots denote earthquakes with magnitudes greater than 1 since 2018 (data were obtained from the Sichuan Earthquake Administration). The cyan triangles show the location of the three dense linear arrays. The color version of this figure is available only in the electronic edition.

movement of river channels and sediment transport could have resulted in deposits hundreds of meters wide and extending to hundreds of meters in depth. Therefore, the LVZ developed along the Anning River may be a reflection of the fluvial scouring and aggrading of the riverbed.

The present shallow LVZ structure in the Anning River Valley was concluded in Figure 10. The fluvial deposition LVZ with a range of ~400–1000 m in width and ~140–200 m in depth was discovered beneath the Anning River. The LVZs distributed beneath the two fault branches were composed of fault-controlled sediment deposits and FDZs. These LVZs were ~1000–1500 m wide and ~300–400 m deep. In addition, a small LVZ existed on the east side of the F_e , which could be associated with sediment deposits controlled by a small, hidden strike-slip fault. This LVZ was measured ~500–700 m in

obtained using different geophysical methods (Ben-Zion *et al.*, 2015; Yang *et al.*, 2020; Jiang *et al.*, 2021; Song and Yang, 2022). These high-resolution imaging results showed that the LVZs were usually a few kilometers under the surface.

With the help of methane detonation sources, three linear dense arrays with apertures of ~8–9 km across the ANHF can greatly assist us in constraining the width and depth of the LVZs. However, first-arrival tomography cannot recover the underground velocity structure deeper than 500 m, as shown in this study. To resolve the subsurface structure at greater depths, we may conduct reflection tomography (Woodward *et al.*, 2008) on the acquired data in future work.

We knew that increasing the length of the dense array would improve our ability to visualize the depth of the LVZs. Nevertheless, due to the limitations of the working

width and ~200 m in depth. Based on the shallow fine structure obtained by ambient noise tomography using an array with larger aperture, Luo *et al.* (2023) inferred that the dip angle of the ANHF zone is ~68° eastward. Our rather shallow structure from the dense small-aperture arrays prevents us from estimating the dip angle in depth. Additional information, such as high-resolution earthquake locations, could help better constrain the fault geometry at depth.

Prospective of the methane detonation source in imaging the depth of the LVZs

There were different perspectives on the depth of the LVZ. At first, across-fault arrays were usually distributed over small apertures (1–2 km) in earlier studies. By studying the trapped waves acquired by such observation system, some scholars concluded that the depth of the LVZ can reach the base of the seismogenic zone (Li and Vernon, 2001). With the increase in the number of seismometers and the distribution aperture, finer subsurface structures can be

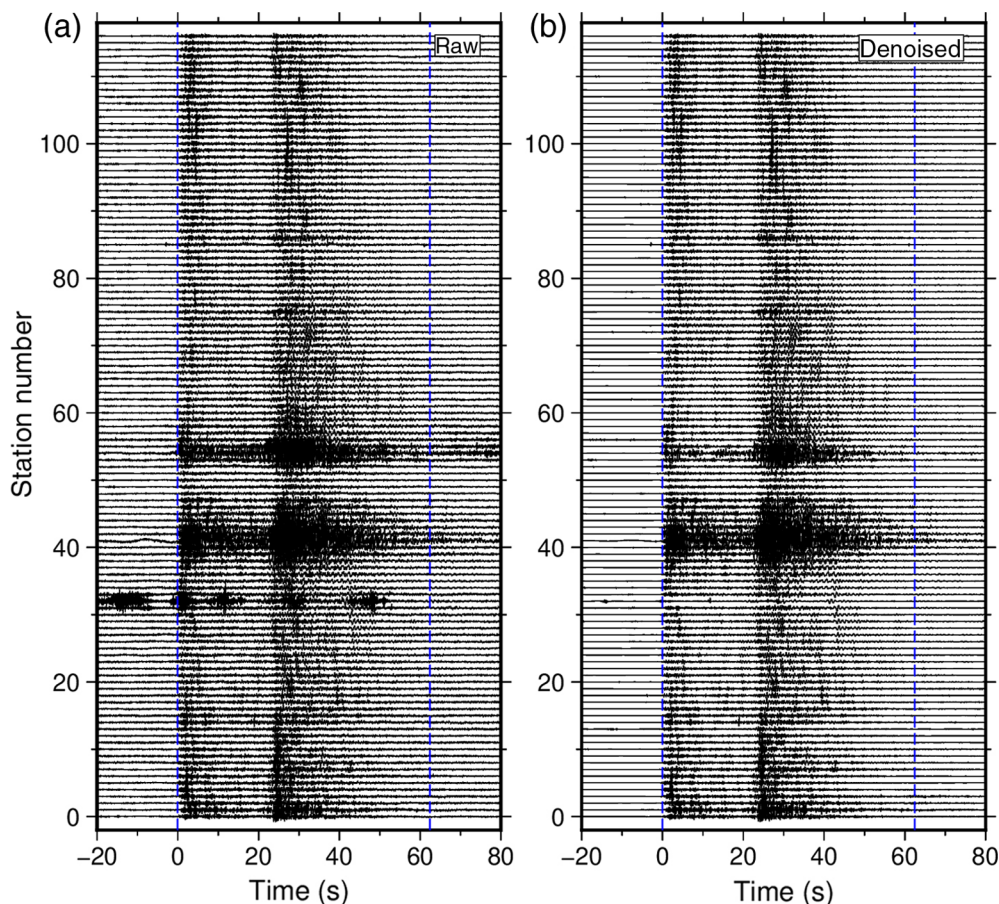


Figure 9. The vertical component aligned with the first P -wave arrival from a local earthquake. Panels (a) and (b) show the field data without and with denoising, respectively. Note that this field data are acquired by array MX1. The color version of this figure is available only in the electronic edition.

environment (i.e., mountains and urban areas), lengthening the dense array was sometimes challenging. According to the source–receiver reciprocity (Betti, 1872), seismic data from deeper layers can be obtained by increasing the number and coverage of sources rather than increasing the length of dense arrays. Theoretical wave propagation path analysis also showed that increasing the number and coverage of seismic sources can improve imaging depth significantly (Fig. S5). In addition, the imaging depth increased with source coverage length. The emergence of methane detonation sources, which have the characteristics of being pollution-free, high-construction efficiency, and low cost, made it possible to investigate the depth of LVZs using a large number of sources.

The influence of LVZs on future seismic hazard

Many studies demonstrated that a large earthquake is likely to strike the Mianning–Xichang segment of the ANHF in the near future (Wen, Fan, *et al.*, 2008; Wen, Ma, *et al.*, 2008; Ran *et al.*, 2008). Based on the cumulative seismic moment, Wen, Fan, *et al.* (2008) estimated the maximum magnitude of the potential earthquake in the Mianning–Xichang segment to be 7.4. By

conducting dynamic rupture simulations, Yao and Yang (2022) predicted the moment magnitude to be 6.9–7.3 in the ANHF, depending on where the rupture nucleated.

Our imaging results showed a large velocity difference between the LVZs beneath the fault traces and the surrounding rocks. When the seismic wave propagates through the LVZs, strong reflections and multiple reflections between the intact rock and the LVZs will be generated. As a result, the rupture velocity can oscillate as a result of the reflected waves, resulting in multiple slip pulses and significant ground damage (Huang and Ampuero, 2011). In addition, these densely distributed LVZs may greatly promote surface rupture and slip of the ANHF, as well as amplifying the ground motion (Weng *et al.*, 2016; Song and Yang, 2022; Yao and Yang, 2023). Considering the large population living in the the Anning River Valley, the risks of future strong earthquakes and LVZ-amplified

ground motions must be taken into account in assessing seismic hazard in the region.

Conclusions

We acquired three seismic datasets using 28 methane detonation sources and three linear dense arrays deployed across the ANHF in Sichuan, China. Using the first arrivals of these three datasets for tomographic imaging, three high-resolution shallow P -wave velocity models within a depth of ~ 500 m were obtained. The three tomographic imaging results revealed LVZs with a depth of ~ 300 – 400 m, a width of ~ 1000 – 1500 m, and a velocity reduction of at least 31% beneath the mapped surface fault traces. We interpreted the LVZs as a combined result of FDZs produced by historical earthquakes and sedimentation processes controlled by the ANHF. In the Anning River Valley, where agriculture was developed and the population was large, the newly discovered wide LVZs can be used as an important basis for future earthquake risk assessment, because they may play critical roles in rupture propagation and amplify the ground motion during future earthquakes. Furthermore, our experiments demonstrated that the environmentally friendly methane detonation

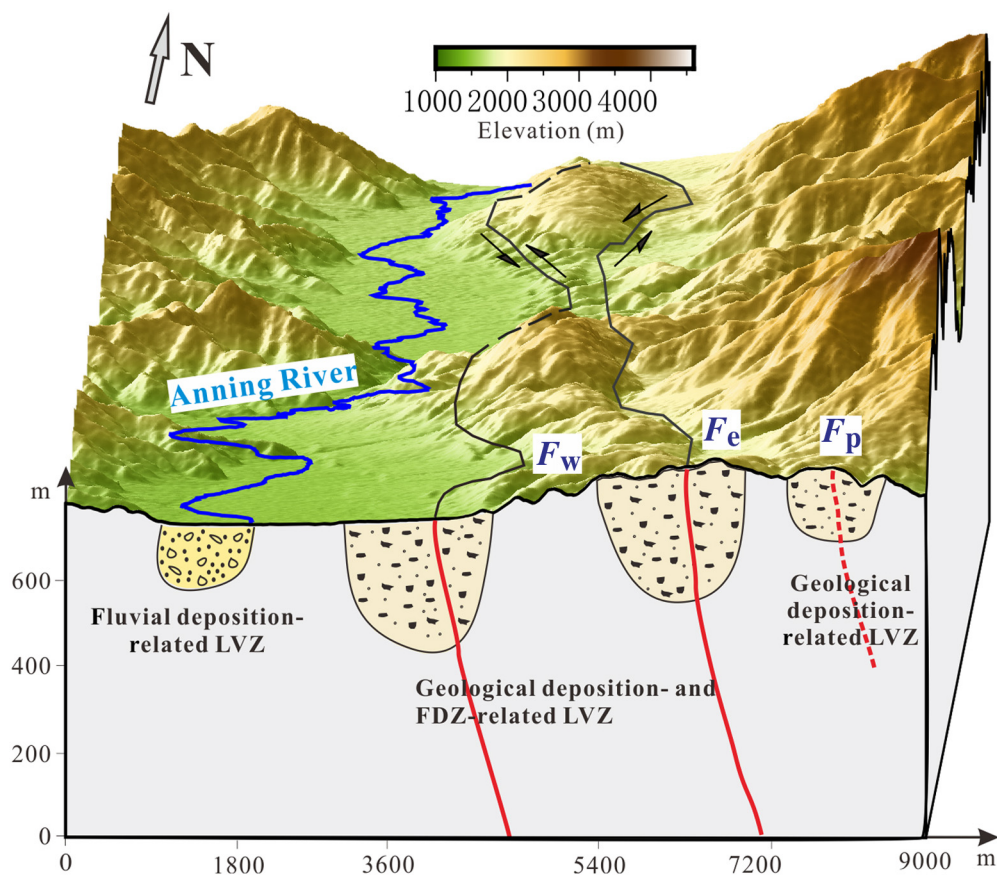


Figure 10. Schematic illustration of the LVZs beneath the Anning River Valley. Note that the fault dip depicted in the diagram is not the real case. The color version of this figure is available only in the electronic edition.

source and linear dense arrays were effective for imaging shallow crustal structures in complex environments such as cities and mountains.

Data and Resources

The acquired raw data, picked *P*-wave first-arrival times, and tomographic results are available at <https://figshare.com/s/3066cd7db34cbe32fa60> (last accessed August 2023). Details of the shot locations and timing, initial models, checkerboard tests and results can be found in the supplemental material.

Declaration of Competing Interests

The authors acknowledge that there are no conflicts of interest recorded.

Acknowledgments

This study is supported by the National Key R&D Program of China (Grant Number 2018YFC1503400), National Outstanding Youth Science Foundation (Grant Number 41922028), Hong Kong Research Grant Council Grants (Grant Numbers 14306119 and 14306418), China Earthquake Science Experiment Project, China Earthquake Administration (CEA; Grant Number 2018CSES0102), State Key Lab of Earthquake Dynamics (Grant Number LED2021B03), and The

Open Foundation of the United Laboratory of Numerical Earthquake Forecasting (Grant Number 2021LNEF02). The authors thank J. W. Huang for sharing the PFAST code used in this study, which is open on GitHub (<https://github.com/junwei-h/PFAST>, last accessed February 2023). H. Chen, J. P. Zi, and S. L. Yao from the Chinese University of Hong Kong are also thanked for their discussion and suggestions on this work. All figures are produced using Generic Mapping Tools (GMT), MATLAB (www.mathworks.com/products/matlab, last accessed August 2023), and CorelDRAW. The authors thank the editor and anonymous reviewers for their constructive comments that help improve the article.

References

- Allam, A. A., Y. Ben-Zion, I. Kurzon, and F. Vernon (2014). Seismic velocity structure in the Hot Springs and trifurcation areas of the San Jacinto Fault zone, California, from double-difference tomography, *Geophys. J. Int.* **198**, 978–999.
- An, Y., D. Wang, Q. Ma, Y. Xu, Y. Li, Y. Zhang, Z. Liu, C. Huang, J. Su, J. Li, *et al.* (2023). Preliminary report of the September 5, 2022 MS 6.8 Luding earthquake, Sichuan, China, *Earthq. Res. Adv.* **3**, no. 1, 100184, doi: [10.1016/j.eqrea.2022.100184](https://doi.org/10.1016/j.eqrea.2022.100184).
- Ben-Zion, Y., and C. G. Sammis (2003). Characterization of fault zones, *Pure Appl. Geophys.* **160**, 677–715.
- Ben-Zion, Y., Z. G. Peng, D. Okaya, L. Seeber, J. G. Armbruster, N. Ozer, A. J. Michael, S. Baris, and M. Aktar (2003). A shallow fault-zone structure illuminated by trapped waves in the Karadere-Duzce branch of the North Anatolian fault, western Turkey, *Geophys. J. Int.* **152**, 699–717.
- Ben-Zion, Y., F. L. Vernon, Y. Ozakin, D. Zigone, Z. E. Ross, H. Meng, M. White, J. Reyes, D. Hollis, and M. Barklage (2015). Basic data features and results from a spatially dense seismic array on the San Jacinto fault zone, *Geophys. J. Int.* **202**, 370–380.
- Betti, E. (1872). Teoria dell'elasticità: Il Nuovo Cimento, *Sezione 6*, nos. 7/8, 87–97.
- Bleibinhaus, F., J. A. Hole, T. Ryberg, and G. S. Fuis (2007). Structure of the California Coast ranges and San Andreas Fault at SAFOD from seismic waveform inversion and reflection imaging, *J. Geophys. Res.* **112**, no. B6, B06315, doi: [10.1029/2006JB004611](https://doi.org/10.1029/2006JB004611).
- Chen, X., and H. Yang (2020). Effects of seismogenic width and low-velocity zones on estimating slip-weakening distance from near-fault ground deformation, *Geophys. J. Int.* **223**, 1497–1510.

- Chen, Z. Q., H. J. Yao, X. H. Shao, S. Luo, and H. F. Yang (2023). Detailed sedimentary structure of the Mianning segment of the Anninghe fault zone revealed by H/V spectral ratio, *Earthq. Res. Adv.* **3**, 100232, doi: [10.1016/j.eqrea.2023.100232](https://doi.org/10.1016/j.eqrea.2023.100232).
- Cheng, J. W., G. H. Guo, and Z. J. Yue (2010). Basic characteristics and earthquake risk analysis of the Anning River fault zone in the west of Sichuan Province, *J. Seismol. Res.* **33**, 265–272.
- Cochran, E. S., Y. G. Li, P. M. Shearer, S. Barbot, Y. Fialko, and J. E. Vidale (2009). Seismic and geodetic evidence for extensive, long-lived fault damage zones, *Geology* **37**, 315–318.
- Faulkner, D. R., C. A. L. Jackson, R. J. Lunn, R. W. Schlische, Z. K. Shipton, C. A. J. Wibberley, and M. O. Withjack (2010). A review of recent developments concerning the structure, mechanics and fluid flow properties of fault zones, *J. Struct. Geol.* **32**, 1557–1575.
- Harris, R. A., and S. M. Day (1997). Effects of a low-velocity zone on a dynamic rupture, *Bull. Seismol. Soc. Am.* **87**, 1267–1280.
- Hu, Y., Z. Li, R. Liu, and Z. Wang (2023). Focal mechanism of Luding M 6.8 earthquake, September 2022 and analysis of the loading role of the tectonic stress on the seismogenic fault, *Earthq. Res. Adv.* **3**, no. 3, 100216, doi: [10.1016/j.eqrea.2023.100216](https://doi.org/10.1016/j.eqrea.2023.100216).
- Huang, Y., and J. P. Ampuero (2011). Pulse-like ruptures induced by low-velocity fault zones, *J. Geophys. Res.* **116**, no. B12, B12307, doi: [10.1029/2011JB008684](https://doi.org/10.1029/2011JB008684).
- Huang, J. W., and G. Bellefleur (2012). Joint transmission and reflection traveltimes tomography using the fast sweeping method and the adjoint-state technique, *Geophys. J. Int.* **188**, 570–582.
- Hole, J. A., T. Ryberg, G. S. Fuis, F. Bleibinhaus, and A. K. Sharma (2006). Structure of the San Andreas Fault Zone at SAFOD from a seismic refraction survey, *Geophys. Res. Lett.* **33**, L07312, doi: [10.1029/2005GL025194](https://doi.org/10.1029/2005GL025194).
- Ji, Z. B., Z. X. Li, R. Z. He, X. Niu, and W. Wu (2021). Seismic signal characteristics of a new source based on methane gaseous detonation in the Tibetan Plateau, *Acta Geosci. Sin.* **43**, 224–234 (in Chinese).
- Jiang, G., X. Xu, G. Chen, Y. Liu, Y. Fukahata, H. Wang, G. Yu, X. Tan, and C. Xu (2015). Geodetic imaging of potential seismogenic asperities on the Xianshuihe-Anninghe-Zemuhe fault system, southwest China, with a new 3-D viscoelastic interseismic coupling model, *J. Geophys. Res.* **120**, 1855–1873.
- Jiang, X., S. Hu, and H. Yang (2021). Depth extent and V_p/V_s ratio of the Chenghai fault zone, Yunnan, China constrained from dense-array-based teleseismic receiver functions, *J. Geophys. Res.* **126**, e2021JB022190, doi: [10.1029/2021JB022190](https://doi.org/10.1029/2021JB022190).
- Kurzban, I., F. L. Vernon, Y. Ben-Zion, and G. Atkinson (2014). Ground motion prediction equations in the San Jacinto fault zone: Significant effects of rupture directivity and fault zone amplification, *Pure Appl. Geophys.* **171**, 3045–3081.
- Lay, V., S. Buske, S. B. Bodenbunrg, J. Townend, R. Kellett, M. K. Savage, D. R. Schmitt, A. Constantinou, J. D. Eccles, M. Bertram, *et al.* (2020). Seismic P wave velocity model from 3-D surface and borehole seismic data at the Alpine Fault DFD-2 drill site (Whataroa, New Zealand), *J. Geophys. Res.* **125**, e2019JB018519, doi: [10.1029/2019JB018519](https://doi.org/10.1029/2019JB018519).
- Lewis, M. A., Z. G. Peng, Y. Ben-Zion, and F. L. Vernon (2005). Shallow seismic trapping structure in the San Jacinto Fault Zone near Anza, California, *Geophys. J. Int.* **162**, 867–881.
- Li, H., H. Wang, Z. Xu, J. Si, J. Pei, T. Li, Y. Huang, S. R. Song, L. W. Kuo, Z. Sun, *et al.* (2013). Characteristics of the fault-related rocks, fault zones and the principal slip zone in the Wenchuan earthquake fault scientific drilling project Hole-1 (WFSD-1), *Tectonophysics* **584**, 23–42.
- Li, H., L. Zhu, and H. Yang (2007). High-resolution structures of the Landers fault zone inferred from aftershock waveform data, *Geophys. J. Int.* **171**, no. 3, 1295–1307, doi: [10.1111/j.1365-246X.2007.03608.x](https://doi.org/10.1111/j.1365-246X.2007.03608.x).
- Li, L., H. Yao, S. Luo, J. Li, X. Wang, H. Ni, and Z. Bao (2021). A multi-scale 3-D crust velocity model in the Hefei-Chao Lake area around the southern segment of Tanlu Fault Zone, *Earthq. Sci.* **34**, no. 4, 344–357, doi: [10.29382/eqs-2021-0020](https://doi.org/10.29382/eqs-2021-0020).
- Li, Y., J. E. Vidale, S. M. Day, and D. D. Oglesby (2002). Study of the 1999 M 7.1 Hector Mine, California, earthquake fault plane by trapped waves, *Bull. Seismol. Soc. Am.* **92**, 1318–1332.
- Li, Y. G., and P. E. Malin (2008). San Andreas fault damage at SAFOD viewed with fault-guided waves, *Geophys. Res. Lett.* **35**, L08304, doi: [10.1029/2007GL032924](https://doi.org/10.1029/2007GL032924).
- Li, Y. G., and F. L. Vernon (2001). Characterization of the San Jacinto Fault Zone near Anza, California, by fault zone trapped waves, *J. Geophys. Res.* **106**, no. B12, 30,671–30,688.
- Luan, Y., H. Yang, B. Wang, W. Yang, W. Wang, J. Yang, X. Li, and J. Ran (2023). Seasonal variations of seismic travel time changes in Binchuan, southwestern China, inferred from large volume air-gun source array data, *Seismol. Res. Lett.* doi: [10.1785/0220220200](https://doi.org/10.1785/0220220200).
- Luo, S., H. J. Yao, J. Wen, H. F. Yang, B. F. Tian, and M. X. Yan (2023). Apparent Low-Velocity Belt in the Shallow Anninghe Fault Zone in SW China and Its Implications for Seismotectonics and Earthquake Hazard Assessment, *J. Geophys. Res.* **128**, e2022JB025681, doi: [10.1029/2022JB025681](https://doi.org/10.1029/2022JB025681).
- McGuire, J., and Y. Ben-Zion (2005). High-resolution imaging of the Bear Valley section of the San Andreas fault at seismogenic depths with fault-zone head waves and relocated seismicity, *Geophys. J. Int.* **163**, 152–164.
- Mousavi, S. M., and C. A. Langston (2016). Hybrid seismic denoising using higher-order statistics and improved wavelet block thresholding, *Bull. Seismol. Soc. Am.* **106**, 1380–1393.
- Peng, Z., Y. Ben-Zion, A. J. Michael, and L. Zhu (2003). Quantitative analysis of seismic fault zone waves in the rupture zone of the landers, 1992, California earthquake: Evidence for a shallow trapping structure, *Geophys. J. Int.* **155**, 1021–1041.
- Pratt, T. L., J. W. Horton Jr, J. Munoz, S. E. Hough, M. C. Chapman, and C. G. Olgun (2017). Amplification of earthquake ground motions in Washington, DC, and implications for hazard assessments in central and eastern North America, *Geophys. Res. Lett.* **44**, 12,150–12,160.
- Qu, Z., B. Zhu, Y. Cao, and H. Fu (2023). Rapid report of seismic damage to buildings in the 2022 M 6.8 Luding earthquake, China, *Earthq. Res. Adv.* **3**, no. 1, 100180, doi: [10.1016/j.eqrea.2022.100180](https://doi.org/10.1016/j.eqrea.2022.100180).
- Ran, Y., L. Chen, J. Cheng, and H. Gong (2008). Late Quaternary surface deformation and rupture behavior of strong earthquake on the segment north of Mianning of the Anninghe fault, *Sci. China Earth Sci.* **51**, 1224–1237.
- Shao, X. H., H. J. Yao, Y. Liu, H. F. Yang, B. F. Tian, and L. H. Fang (2022). Shallow crustal velocity structures revealed by active source tomography and fault activities of the Mianning–Xichang segment of the Anninghe fault zone, Southwest China, *Earth Planet. Phys.* **6**, 204–213.

- Share, P.-E., Y. Ben-Zion, Z. E. Ross, H. Qiu, and F. Vernon (2017). Internal structure of the San Jacinto fault zone at Blackburn Saddle from seismic data of a linear array, *Geophys. J. Int.* **210**, 819–832.
- Smithyman, B. R., and R. M. Clowes (2012). Waveform tomography of field vibroseis data using an approximate 2D geometry leads to improved velocity models, *Geophysics* **77**, R33–R43.
- Song, J., and H. Yang (2022). Seismic site response inferred from records at a dense linear array across the Chenghai fault zone, Binchuan, Yunnan, *J. Geophys. Res.* **127**, e2021JB022710, doi: [10.1029/2021JB022710](https://doi.org/10.1029/2021JB022710).
- Tan, X. L., L. H. Fang, W. L. Wang, and J. P. Wu (2018). Rayleigh wave group velocity tomography with ambient noise in the Anninghe-Zemuhe fault zone and its surrounding areas, *Earthq. Res. China* **34**, 400–413 (in Chinese).
- Virieux, J., and S. Operto (2009). An overview of full-waveform inversion in exploration geophysics, *Geophysics* **74**, WCC127–WCC152.
- Wang, Y., A. Allam, and F.-C. Lin (2019). Imaging the fault damage zone of the San Jacinto Fault near Anza with ambient noise tomography using a dense nodal array, *Geophys. Res. Lett.* **46**, 12,938–12,948.
- Wen, X., J. Fan, G. Yi, Y. Deng, and F. Long (2008). A seismic gap on the Anninghe fault in western Sichuan, China, *Sci. China Earth Sci.* **51**, 1375–1387.
- Wen, X., S. Ma, X. Xu, and Y. He (2008). Historical pattern and behavior of earth-quake ruptures along the eastern boundary of the Sichuan-Yunnan faulted block, southwestern China, *Phys. Earth Planet. In.* **168**, 16–36.
- Wen, X. Z. (2000). Character of rupture segmentation of the xian-shuihe-anninghe-zemuhe fault zone, western Sichuan, *Seismol. Geol.* **22**, 239–249 (in Chinese).
- Weng, H., H. Yang, Z. Zhang, and X. Chen (2016). Earthquake rupture extents and coseismic slips promoted by damaged fault zones, *J. Geophys. Res.* **121**, 4446–4457.
- Woodward, M. J., D. Nichols, O. Zdraveva, P. Whitfield, and T. Johns (2008). A decade of tomography, *Geophysics* **73**, VE5–VE11.
- Wu, C. Q., Z. G. Peng, and Y. Ben-Zion (2009). Non-linearity and temporal changes of fault zone site response associated with strong ground motion, *Geophys. J. Int.* **176**, 265–278.
- Xie, F., C. Liang, S. Dai, B. Shao, H. Huang, J. Ouyang, L. Li, and E. Larose (2023). Preliminary results on a near-real-time rock slope damage monitoring system based on relative velocity changes following the September 5, 2022 MS 6.8 Luding, China earthquake, *Earthq. Res. Adv.* **3**, no. 1, 100202, doi: [10.1016/j.eqrea.2022.100202](https://doi.org/10.1016/j.eqrea.2022.100202).
- Xu, J., K. D. Wang, J. L. Li, N. Gu, N. Ding, J. W. Qian, W. Yang, and H. J. Zhang (2021). High resolution tomography of the Tanlu fault zone near Hefei with passive seismic and magnetotelluric linear array data, *Earthq. Sci.* **34**, no. 1, 24–35, doi: [10.29382/eqs-2020-0061](https://doi.org/10.29382/eqs-2020-0061).
- Yang, H., S. Yao, and X. Chen (2022). Rupture propagation on heterogeneous fault: Challenges for predicting earthquake magnitude, *Chin. Sci. Bull.* **67**, 1–14 (in Chinese).
- Yang, H. F. (2015). Recent advances in imaging crustal fault zones: A review, *Earthq. Sci.* **28**, 151–162.
- Yang, H. F., and L. P. Zhu (2010). Shallow low-velocity zone of the San Jacinto fault from local earthquake waveform modeling, *Geophys. J. Int.* **183**, 421–432.
- Yang, H. F., Y. H. Duan, J. H. Song, X. H. Jiang, X. F. Tian, W. Yang, W. T. Wang, and J. Yang (2020). Fine structure of the Chenghai fault zone, Yunnan, China, constrained from teleseismic travel time and ambient noise tomography, *J. Geophys. Res.* **125**, e2020JB019565, doi: [10.1029/2020JB019565](https://doi.org/10.1029/2020JB019565).
- Yang, H. F., Y. H. Duan, J. H. Song, W. T. Wang, W. Yang, X. F. Tian, and B. S. Wang (2021). Illuminating high-resolution crustal fault zones and temporal changes using multi-scale dense arrays and airgun sources, *Earthq. Res. Adv.* **1**, 100001, doi: [10.1016/j.eqrea.2021.100001](https://doi.org/10.1016/j.eqrea.2021.100001).
- Yao, S., and H. Yang (2022). Hypocentral dependent shallow slip distribution and rupture extents along a strike-slip fault, *Earth Planet. Sci. Lett.* **578**, 117296, doi: [10.1016/j.epsl.2021.117296](https://doi.org/10.1016/j.epsl.2021.117296).
- Yao, S., and H. Yang (2023). Towards ground motion prediction for potential large earthquakes from interseismic locking models, *Earth Planet. Sci. Lett.* **601**, 117905, doi: [10.1016/j.epsl.2022.117905](https://doi.org/10.1016/j.epsl.2022.117905).
- Yehya, A., Z. Yang, and J. R. Rice (2018). Effect of fault architecture and permeability evolution on response to fluid injection, *J. Geophys. Res.* **123**, 9982–9997.
- Yi, G. X., X. Z. Wen, J. Fan, and S. W. Wang (2004). Assessing current faulting behaviors and seismic risk of the anninghe-zemuhe fault zone from seismicity parameters, *Acta Seismol. Sin.* **26**, 294–303 (in Chinese).
- Zhang, Y., H. Yang, W. Yang, W. Wang, and X. Ma (2023). Along-strike variation in the shallow velocity structure beneath the Chenghai Fault Zone, Yunnan, China, constrained from methane sources and dense arrays, *Seismol. Res. Lett.* **94**, 2273–2290, doi: [10.1785/0220230034](https://doi.org/10.1785/0220230034).
- Zhang, Y. Q., N. Yang, H. Meng, and W. Chen (2004). Late Cenozoic tectonic deformation history and uplift process of the Panxi region, western Sichuan, *Geol. China* **31**, 23–33 (in Chinese).
- Zigone, D., Y. Ben-Zion, M. Lehujeur, M. Campillo, G. Hillers, and F. L. Vernon (2019). Imaging subsurface structures in the San Jacinto fault zone with high-frequency noise recorded by dense linear arrays, *Geophys. J. Int.* **217**, 879–893.

Manuscript received 4 May 2023
Published online 10 October 2023